Solid State Communications 372 (2023) 115300

Contents lists available at ScienceDirect

Solid State Communications

journal homepage: www.elsevier.com/locate/ssc

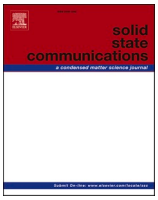

High harmonic generations in GaAs/AlGaAs superlattice: Effect of electric and magnetic field

E. Ozturk [a,*], D. Altun [b,c], O. Ozturk [d], B.O. Alaydin [b,c]

[a] Department of Physics, Sivas Cumhuriyet University, 58140, Sivas, Turkey
[b] Nanophotonic Application and Research Center, Sivas Cumhuriyet University, 58140, Sivas, Turkey
[c] Sivas Vocational College, Sivas Cumhuriyet University, 58140, Sivas, Turkey
[d] Department of Nanotechnology Engineering, Sivas Cumhuriyet University, 58140, Sivas, Turkey

ARTICLE INFO

Communicated by Francois Peeters

Keywords:
Superlattice
Nonlinear optical rectification (NOR)
Second harmonic generation (SHG)
Third harmonic generation (THG)
Electric field
Magnetic field

ABSTRACT

In this study, we have examined the nonlinear optical rectification (NOR), the second harmonic generation (SHG), and the third harmonic generation (THG) coefficients of the $Al_xGa_{1-x}As/GaAs$ superlattice with a periodically increased barrier width under magnetic field (B) and electric field (F). All calculations are completed using the finite element method under the effective mass approximation. The electric field's polarity (±) changes the probability density of wavefunctions. For B = 0, F = −5 kV/cm (particularly for the difference between energy levels (E_{fi})) is a critical value. Whereas the E_{fi} value decreases between −40 <F < −5 kV/cm, then it increases in the range of −5<F < 40 kV/cm. This change causes a red or blue shift in the optical spectrum. We also see that F = 40 kV/cm causes a change in the transition energies of the structure more than F = −40 kV/cm. The confinement of electrons under applied magnetic fields occurs in the center of the superlattice. The NOR, SHG, and THG coefficients can be adjusted over a wide energy range and size of the resonance peak with changes in the F and B values. It is believed that with the combined effect of the electric and magnetic fields, the electro-optical properties of the superlattices can be tuned for the desirable property of semiconductor optical device applications.

1. Introduction

THz light sources have been very attractive due to their applications in astronomy, environmental monitoring, and security [1–3]. In these applications, the most important part is the THz sources. Up to 2005, gas lasers were the main source of the THz radiation but they were not suitable for wavelength tunability and they were bulky. To overcome these difficulties, a lot of effort has been spent. Microwave oscillators have been investigated but only microwatt-level output power was generated at 1.9 THz [4]. Frequency down-conversion has been still under consideration to generate THz sources and up to now, only a few milliwatt output power is obtained [5]. Another focus of the studies was on the emission properties of the single crystal p-type germanium which did not show high performances [6]. Finally, a quantum cascade laser (QCL) was demonstrated [7]. Since then, it has been seen that QCLs are the most promising approach with their output power in watt level at liquid nitrogen operation temperatures [8]. Even though many efforts, the lack of really efficient and room temperature operating THz sources have still been absent. Beyond the above approaches, high harmonic generations, based on intraband transition, can be suitable for THz sources. In the literature, high harmonic generation has been the main issue of the quantum well (QW), wire, and dot structures. It has been shown that THz radiation can be obtained via the intrasubband transition of electrons between minibands in the conduction band.

Linear and non-linear intersubband transition-related optical properties of low-dimensional nano-sized structures have long been evaluated to provide strong quantum confinement that causes small energy differences in energy levels (ELs) and dipole moment matrix elements (DMMEs) [9–12]. All this is due to the great importance of these structures, which is used in photonic-optoelectronic device technology in the infrared region. It is well known in the literature that DMMEs can indicate large nonlinear behaviors in the QW. Thus, it is crucial to study the second-harmonic and third-harmonic nonlinearities [13,14]. Recently, many studies have been published on the nonlinear optical rectification (NOR), the second harmonic generation (SHG), and the third harmonic generation (THG) coefficients of low-dimensional

* Corresponding author.
E-mail address: eozturk@cumhuriyet.edu.tr (E. Ozturk).

https://doi.org/10.1016/j.ssc.2023.115300
Received 19 April 2023; Received in revised form 17 July 2023; Accepted 7 August 2023
Available online 8 August 2023
0038-1098/© 2023 Elsevier Ltd. All rights reserved.

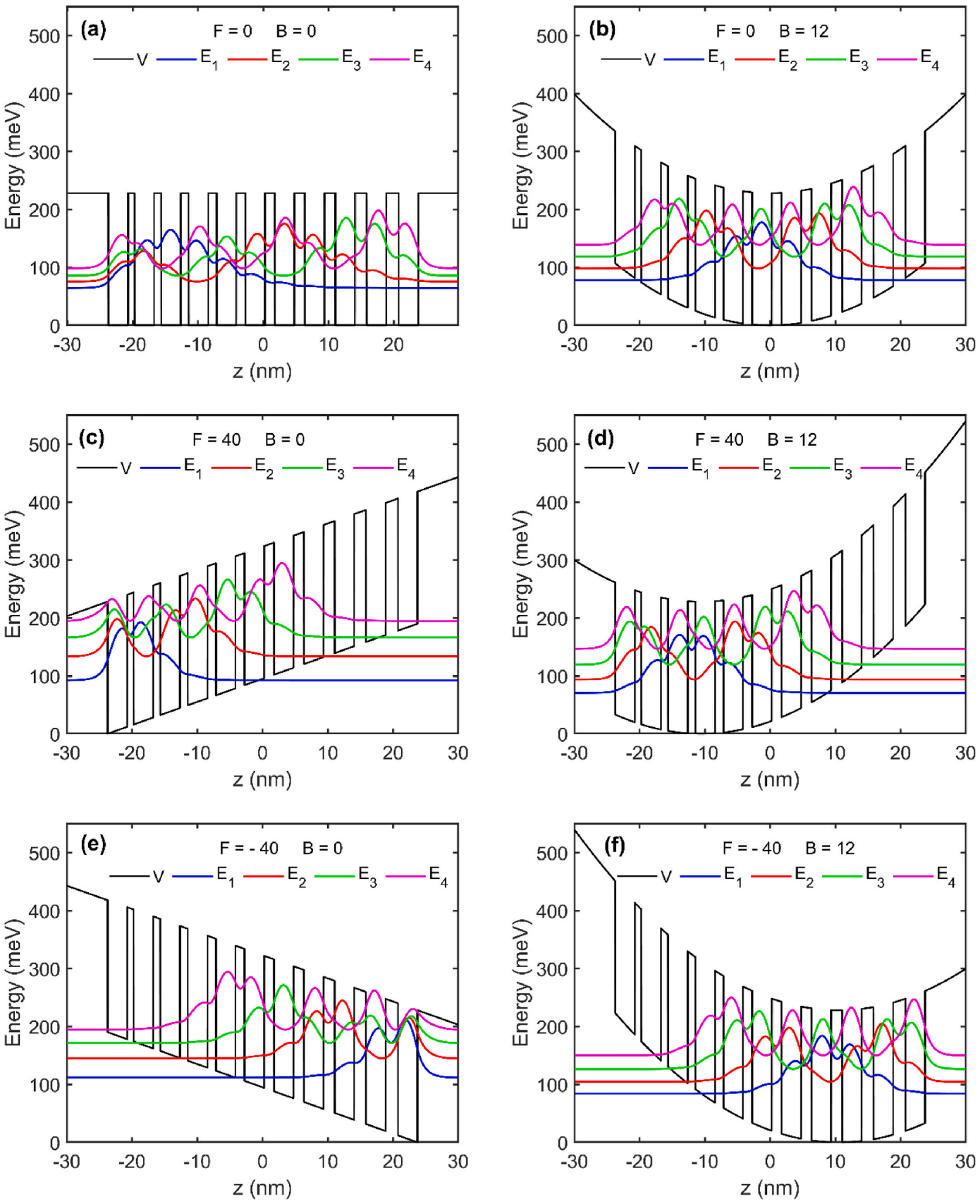

Fig. 1. The potential profiles and the first four electron energy levels corresponding to the associated PD of wavefunctions for a) F = 0; B = 0, b) F = 0; B = 12T, c) F = 40 kV/cm; B = 0, d) F = 40 kV/cm; B = 12 T, e) F = −40 kV/cm; B = 0 and f) F = −40 kV/cm; B = 12T.

nano-sized structures [15–22]. Electronic band structure and NOR in a quantum dot under external fields have been shown by Baskoutas [23]. The THG in cylindrical parabolic quantum wires under an applied electric field has been studied by Wang and Guo [24]. Yu et al. have investigated optical rectification in a one-dimensional quantum dot [25]. Khordad has focused on SHG and THG for quantum wires [26]. The effect of a magnetic field on THG has been detailed for quantum wires by Guo et al. [27]. The electric field control of the optical SHG in a QW has been shown by Tsang et al. [28]. The SHG has been investigated for asymmetric double semi-parabolic QWs under hydrostatic pressure, electric and magnetic field [29]. The NOR and SHG have been considered for Gaussian potential [19,30]. GaAs delta-doped FET system is used to simulate the NOR, SHG, and THG by Martine-Orozco et al. [17]. Even though published many studies about harmonic generations from low dimensional systems, superlattices are not studied at all. It is very well known in the literature that superlattices have shown superior optical properties and are comparatively better than QW. We have shown in our recent study that superlattices are suitable hetero-structures for high absorption/emission devices under magnetic and electric fields [31].

In this study, we have considered the NOR, SHG, and THG for the AlGaAs/GaAs superlattice which has periodically increased quantum barrier width (BW). The NOR, SHG, and THG coefficients have been calculated under external fields: electric and magnetic fields. As far as we know, this is the first research that comprehensively analyzes the optical properties of a superlattice with different barrier widths. The order of the paper is; theory is described in section II with equations. The parameters used in the study, research results, and discussion are presented in section III. We have finished the paper with a conclusion given in section IV.

2. Theory

Time-independent Hamiltonian of the $Al_xGa_{1-x}As/GaAs$ superlattice with periodically increased barrier width is given in Eq. (1). The finite element method, which is a numerical calculation method based on matrix diagonalization and very well known in the literature [32–34], is used to calculate the wave functions (WFs) and their corresponding ELs under the effective mass approximation.

$$H = -\frac{\hbar^2}{2m^*}\frac{d^2}{dz^2} + \frac{e^2B^2z^2}{2\,m^*c^2} + e\,F\,z + V(z) \tag{1}$$

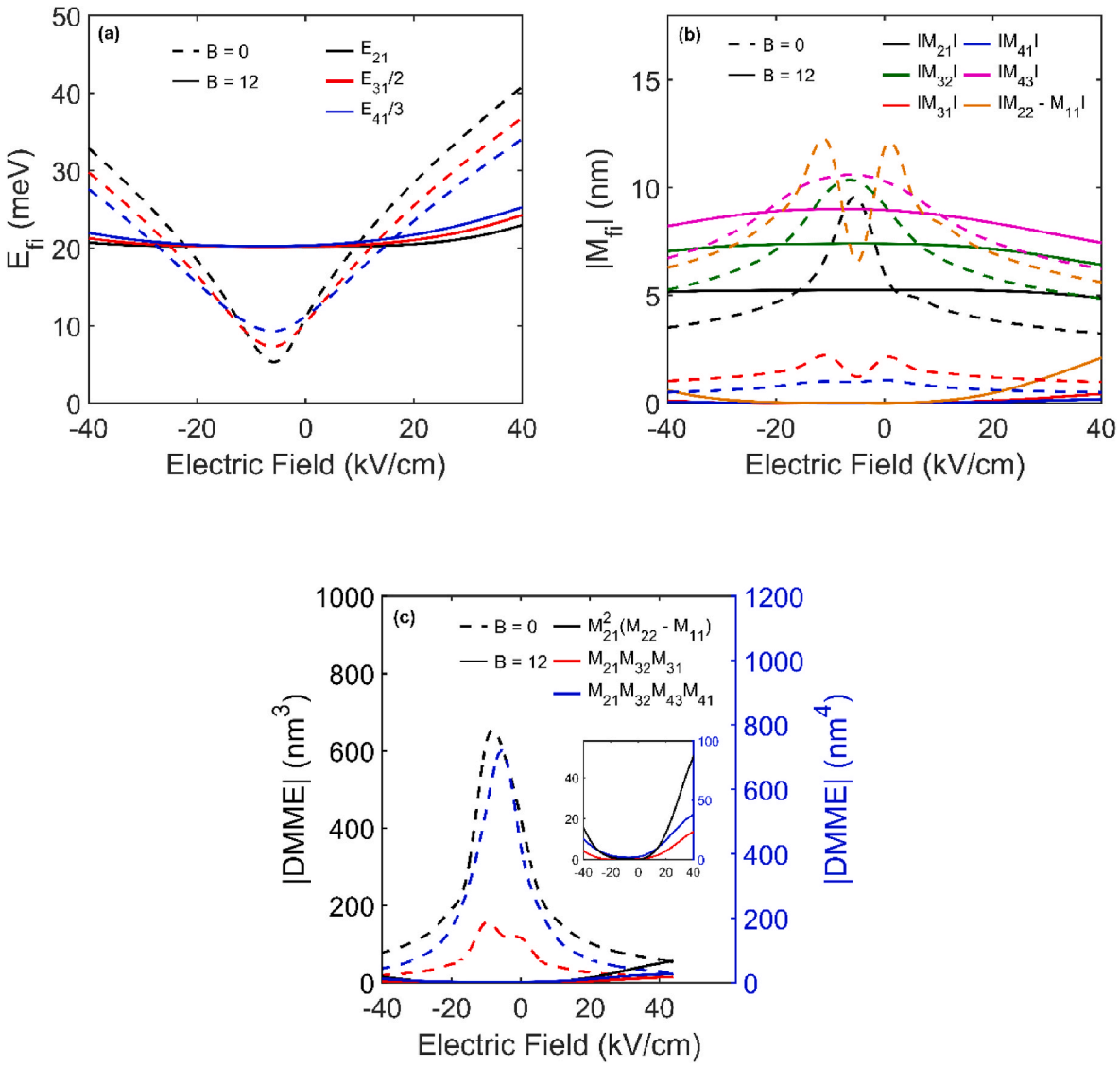

Fig. 2. a) Transition energies, b) DMMEs, and c) Products of the DMMEs (the inset shows the DMME products for B = 12 T) as a function of electric field for B = 0 and B = 12T.

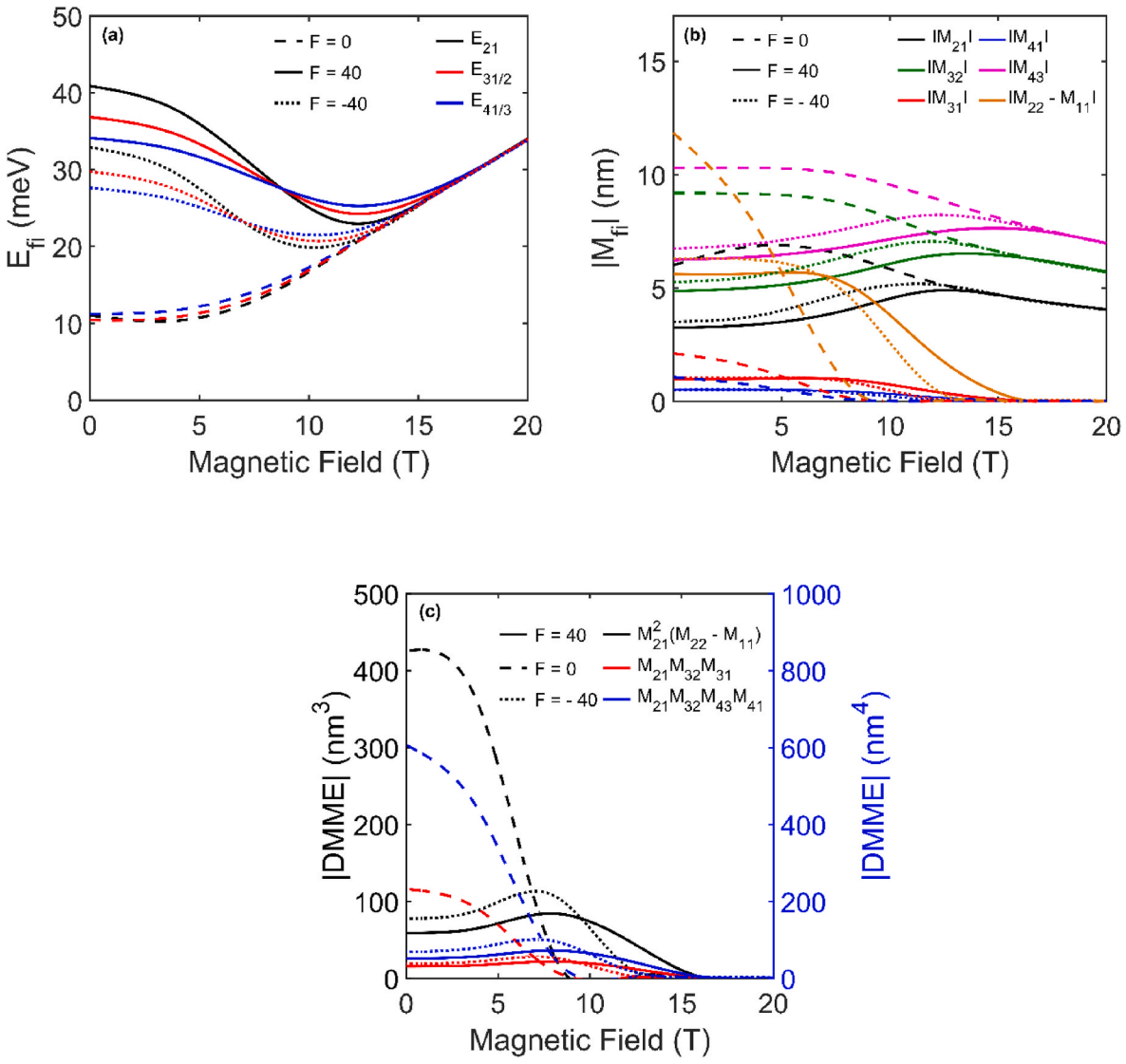

Fig. 3. a) Transition energies, b) DMMEs, and c) Product of DMMEs as a function of magnetic field for F = 0 and F = ±40 kV/cm.

where Hamiltonian contains a second-order differential equation and it is solved by diagonalization [35].

$$\frac{d^2}{dz^2} = [-2\,\mathrm{diag}(\mathrm{ones}(1,N_z)) + \mathrm{diag}(\mathrm{ones}(1,N_z-1),-1) + \mathrm{diag}(\mathrm{ones}(1,N_z-1),1)]^2 \tag{2}$$

In Eq. (1), the effective mass of the electron, the electron charge, the length of the matrix, the electric field (in the growth direction), the magnetic field (perpendicular to the growth direction), and the confined potential are represented respectively as m^*, e, N_z, F, B, and $V(z)$. For the potential profile of the superlattice designed with eleven QWs, the leftmost BW is 1 nm, and the rightmost BW is 2 nm by increasing 0.1 nm to the right. The barrier width intentionally is chosen as 1 nm which is the experimental limitation of the growth techniques. The well widths are 3 nm and are kept constant across the whole superlattice.

After the WFs and corresponding ELs, NOR, SHG, and THG coefficients have been calculated under the compact density matrix approach [36,37].

$$\chi_0^{(2)} = \frac{4e^3\sigma_v}{\varepsilon_o} M_{21}^2 \delta_{21} \frac{E_{21}^2\left(1+\frac{\Gamma_2}{\Gamma_1}\right) + \hbar^2(\omega^2+\Gamma_2^2)\left(\frac{\Gamma_2}{\Gamma_1}-1\right)}{\left((E_{21}-\hbar\omega)^2+(\hbar\Gamma_2)^2\right)\left((E_{21}+\hbar\omega)^2+(\hbar\Gamma_2)^2\right)} \tag{3}$$

$$\chi_{2\omega}^{(2)} = \frac{e^3\sigma_v}{\varepsilon_o} \frac{M_{21}M_{32}M_{31}}{(\hbar\omega - E_{21} - i\hbar\Gamma_3)(2\hbar\omega - E_{31} - i\hbar\Gamma_3/2)} \tag{4}$$

$$\chi_{3\omega}^{(3)} = \frac{e^4\sigma_v}{\varepsilon_o} \frac{M_{21}M_{32}M_{43}M_{41}}{(\hbar\omega - E_{21} - i\hbar\Gamma_3)(2\hbar\omega - E_{31} - i\hbar\Gamma_3/2)(3\hbar\omega - E_{41} - i\hbar\Gamma_3/3)} \tag{5}$$

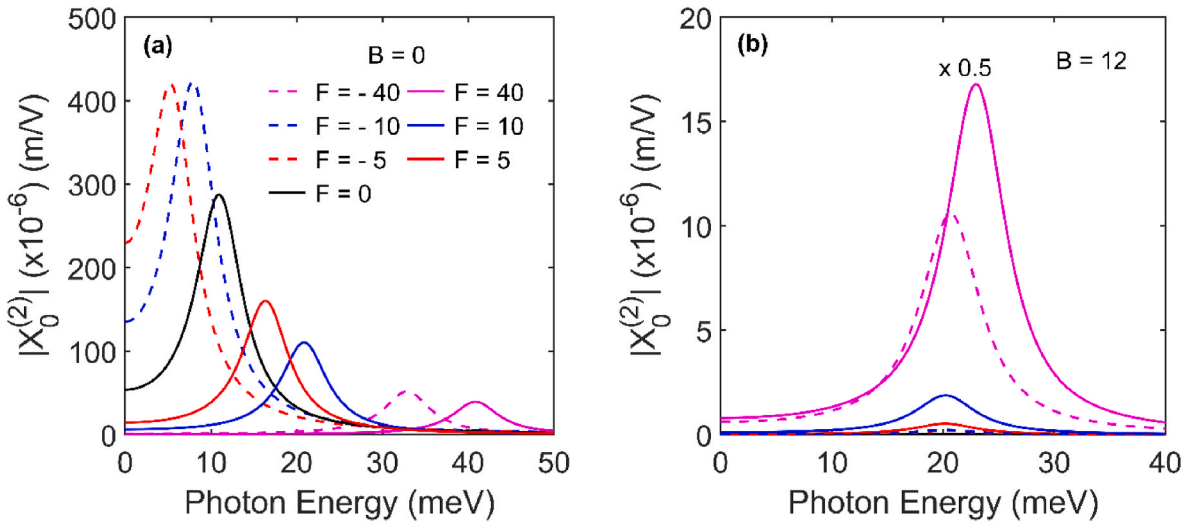

Fig. 4. The NOR coefficient as a function of photon energy under different electric field values for a) B = 0, b) B = 12 T (the curve plotted for F = 40 kV/cm is multiplied by 0.5).

The maxima of the resonance peaks of the NOR, SHG, and THG coefficients are given below.

$$\chi^{(2)}_{0,\max} = \frac{2e^3\sigma_v}{\varepsilon_o \hbar^2 \Gamma_1\Gamma_2} M_{21}^2 \delta_{21} \tag{6}$$

$$\chi^{(2)}_{2\omega,\max} = \frac{e^3\sigma_v}{\varepsilon_o} \frac{M_{21}M_{32}M_{31}}{(\hbar\,\Gamma_3)^2} \tag{7}$$

$$\chi^{(3)}_{3\omega,\max} = \frac{e^4\sigma_v}{\varepsilon_o} \frac{M_{21}M_{32}M_{43}M_{41}}{i(\hbar\,\Gamma_3)^3} \tag{8}$$

M_{fi} describes the DMMEs and it is given as

$$M_{fi} = \int \Psi_f^*\, z\, \Psi_i\, dz, (i, f = 1, 2, 3, 4) \tag{9}$$

where ω is the angular frequency of the photon, ($E_{fi} = E_f - E_i = \hbar\omega_{fi}$), E_f and E_i are the final and initial energy states. $\delta_{21} = M_{22} - M_{11}$ is the intrasubband DMME.

3. Results and discussion

We have considered the NOR, SHG, and THG coefficients in superlattice with and without F and B. In this study, $m^* = 0.067m_0$ (m_0 is the free electron mass), $T_1 = 1/\Gamma_1 = 1$ ps, $T_2 = 1/\Gamma_2 = 0.2$ ps, $T_3 = 1/\Gamma_3 = 0.5$ ps, $\sigma_v = 4x10^{22}m^{-3}$, and the potential height is 228 meV. The F values in the legends of all figures are in kV/cm, and the B values are in T.

The superlattice consists of eleven wells numbered from left to right. Fig. 1(a–f) shows the potential profile, the first four bounded ELs, and the related probability densities (PDs) with and without F and B. The ELs and the PDs of the electrons in the superlattice have been tuned with increasing BW. In the case of zero external field due to asymmetry in BW, electrons in the E_1 level are mostly located between the second and fourth well. Electrons in the E_2 level are observed on the right side of the superlattice. Electrons in the E_3 and E_4 levels are localized along the superlattice region as seen in Fig. 1a. Due to the higher parabolic confinement and DMME effects, the magnetic field of magnitude B = 12 T forces the electrons in the E1 level to be localized in the middle of the superlattice, almost balancing the probability distribution of the E2 level on either side of the superlattice (Fig. 1b). The more energetic electrons in E_3 and E_4 levels show less change under the applied B. As shown in Fig. 1c, the electrons in the E_1 level under the applied F = 40 kV/cm are localized to the left of the superlattice and interaction occurs between the first two wells. Other energy levels also tend to be localized to the left side of the superlattice, as expected due to the tilted structure, and all energy eigenvalues shift to higher energies relative to F = 0. The magnetic field decreases the effect of the electric field and pushes back the electrons to the right of the superlattice when B and F are applied together as shown in Fig. 1d. All energy eigenvalues drop lower than for F = 40 kV/cm and B = 0. When the F direction is changed, the localization of the electrons moves to the right of the superlattice (Fig. 1e). According to the values of F and B in other figures, the energy eigenvalue of E1 reaches its maximum value and the energy difference between the energy levels changes. When B = 12T and F = −40 kV/cm, the energy levels are shifted to the left of the superlattice compared to zero B, and the shift is less pronounced due to thick barriers (Fig. 1f).

Fig. 2 (a, b, and c) shows three energy differences, some of the DMMEs, and three DMME's products dependent on the F values (all DMMEs are taken as absolute values) for B = 0 and B = 12 T. Owing to the shift of the ELs to upper values, the E_{21} transition energy is mostly bigger than $E_{31}/2$ and $E_{41}/3$ for F = ±40 kV/cm and B = 0. The transition energies decrease between −40 kV/cm and −5 kV/cm as shown in Fig. 2a and have the minimum values at −5 kV/cm. After that, the transition energies increased and reached a maximum value of 40 kV/cm due to the asymmetric barrier thickness. A value of B = 12T produces changes in energy levels, but has little effect on energy differences.

As seen in Fig. 2b, M_{21} has a maximum for F = −5 kV/cm and B = 0 due to an increase in the overlap of the PDs. The same behaviors are seen for M_{32} and M_{43}. M_{31} and δ_{21} has a minimum for the value F = −5 kV/cm. However, DMME is almost unchanged for M_{41} owing to the dispersed distribution of the ground energy state and third excited states through the superlattice region. When F and B are applied together, the B eliminates the effect of the F and results in less variation in the transition energies owing to the asymmetric higher confinement. We can say that B balances variation of the transition energies, which is very desired for optoelectronic devices for different operating voltages. The products of DMMEs for B = 0 are higher than B = 12T.

Fig. 3 (a, b, and c) shows the energy differences, DMMEs, and products of DMMEs as a function of B for F = 0 and F = ± 40 kV/cm, respectively. The transition energies proportionally increase with the B intensity for F = 0 because of higher confinement. E_{21}, $E_{31}/2$, and $E_{41}/3$ transition energies are the same for B = 9 T (7 T) for F = 40 kV/cm (−40 kV/cm) intensity. For 40 kV/cm (−40 kV/cm), these transition energies have the minimum at B = 12 T (10 T). E_{21}, $E_{31}/2$, and $E_{41}/3$ transition energies are the same for B = 20 T with/without F. This is a direct result

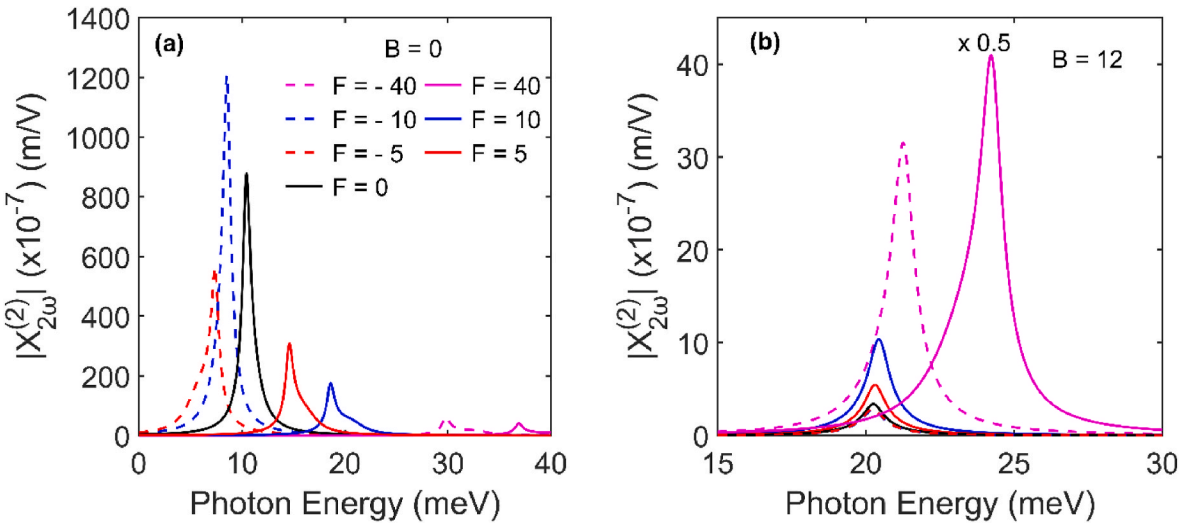

Fig. 5. The SHG coefficients as a function of photon energy under different F intensities for a) B = 0, b) B = 12 T (the curve plotted for F = 40 kV/cm is multiplied by 0.5).

Table 1
Transition energies and maximum values of the NOR, SHG, and THG coefficients for different F and B values.

B (T)	F (kV/cm)	$E_{21} - E_{31}/2$ (meV)	$E_{31}/2 - E_{41}/3$ (meV)	$E_{21} - E_{41}/3$ (meV)	$\chi^{(2)}_{0,max}$ ($\times 10^{-6}$) (m/V)	$\chi^{(2)}_{2\omega,max}$ ($\times 10^{-7}$) (m/V)	$\chi^{(3)}_{3\omega,max}$ ($\times 10^{-13}$) (m/V)^2
0	0	0.6225	−0.8105	−0.188	283.3720	482.6244	1912.7
	40	4.0255	2.7185	6.744	39.2870	64.4214	155.1429
	−40	3.13	2.156667	5.286667	51.6945	79.2099	198.7814
12	0	−0.012	−0.117	−0.129	0.0318	1.6963	8.4635
	40	−1.2735	−1.02817	−2.30167	33.4740	56.5101	139.9612
	−40	−0.5615	−0.7105	−1.272	10.5262	17.0731	63.4090

of the very high confinement with very high B intensity. For F = 0, DMMEs are in decreasing trend by increasing B value. However, the intensity and direction of the F have less impact on DMMEs than F = 0 intensity with increasing B. The products of DMMEs are more pronounced at small B intensities. The energy differences and the DMMEs are also dependent on both F and B intensity for many semiconductor device applications.

For B = 0 and B = 12 T, the NOR coefficient versus the photon energy is plotted in Fig. 4 (a and b) for different F values, respectively. The NOR coefficient is the function of the E_{21}, M_{21}, and δ_{21}, and thus the shift of the NOR coefficient is related to the variation of E_{21} value with changing F. This has a critical point at −5 kV/cm electric field intensity for B = 0 T. If F = 0 is taken as a reference point, while the NOR coefficient a redshift shows up to F = −5 kV/cm, this coefficient shows blueshift between −5 kV/cm and −40 kV/cm. The NOR has a blueshift from 0 to 40 kV/cm and the maxima of the NOR is decreasing in this range with increasing electric field intensity. The maximum of the NOR coefficient is relative to the DMME's product ($|M_{21}|^2|\delta_{21}|$). When comparing F values of the same magnitude, for –F intensities the magnitudes of the

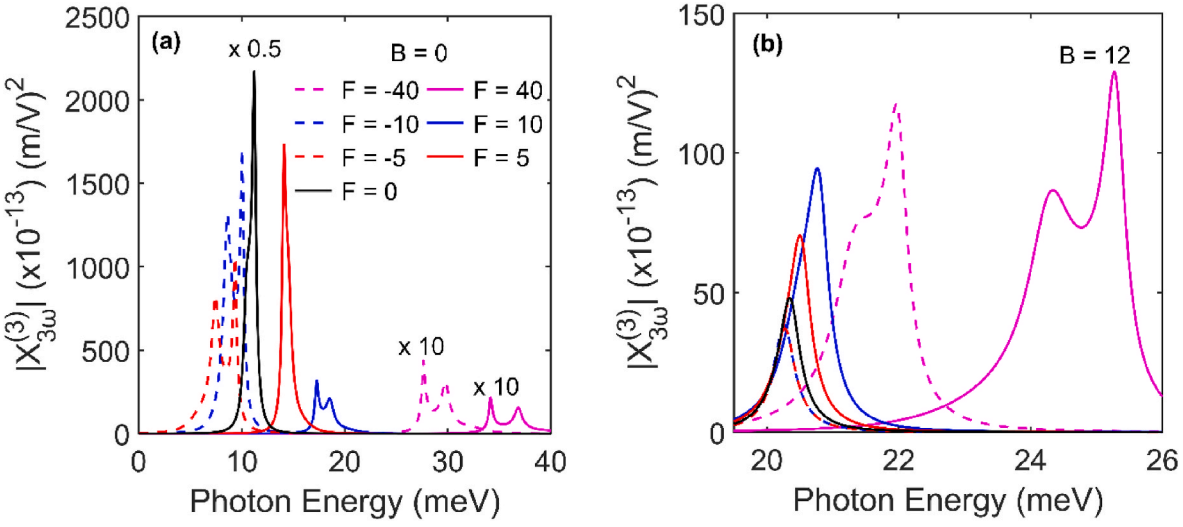

Fig. 6. The THG coefficient as a function of photon energy under different F intensities for a) B = 0 (the curves plotted for F = ± 40 kV/cm are multiplied by 10), b) B = 12 T.

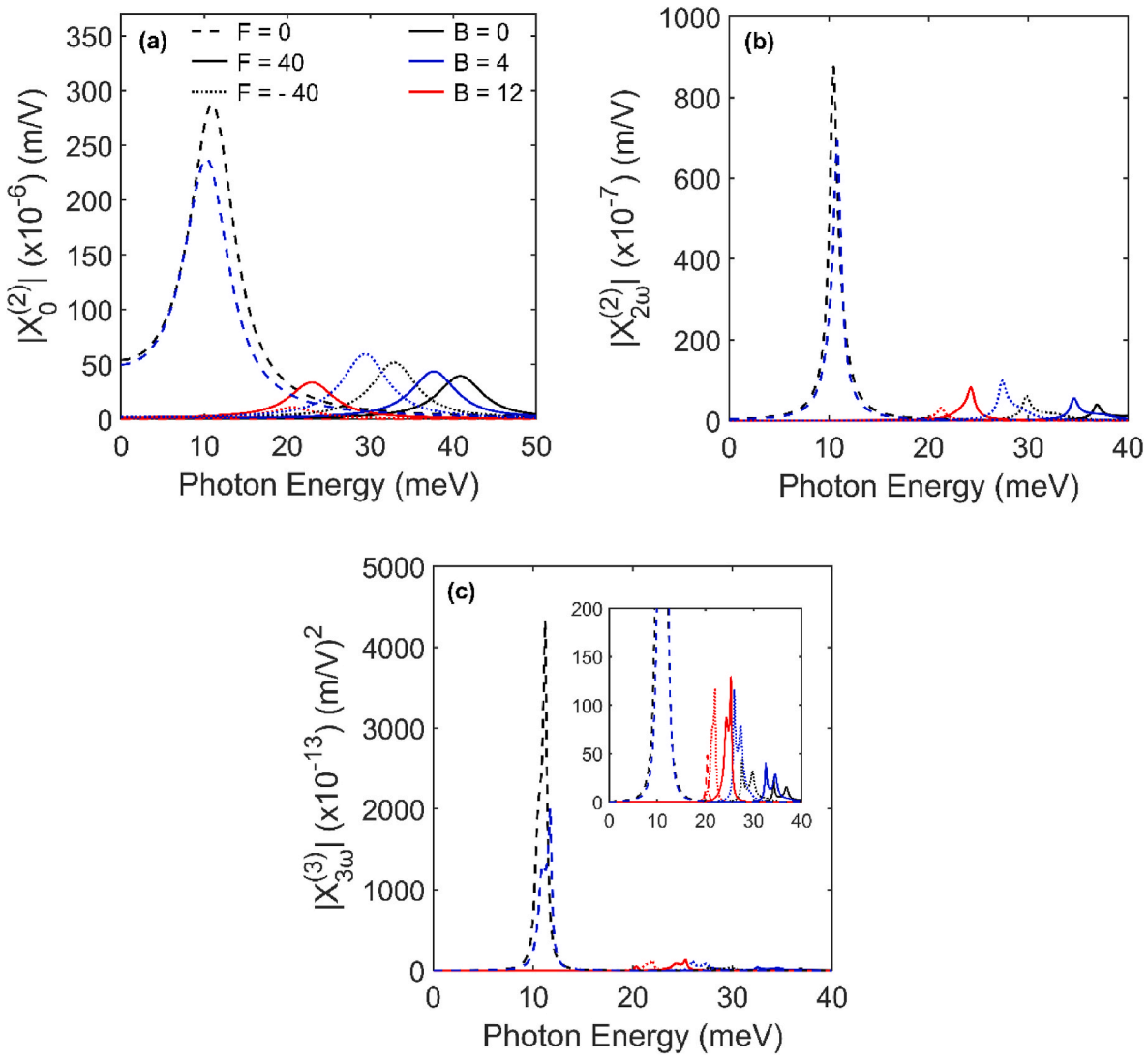

Fig. 7. a) NOR, b) SHG, and c) THG coefficients (the inset shows THG coefficient for different electric and magnetic field values) as a function of photon energy for several electric and magnetic field intensities.

NOR coefficient are higher than + F intensities, but the NOR maxima are at photon energies lower than + F intensities (Fig. 4a). When B = 12 T is applied, the NOR coefficients are quite lower than B = 0 T. The NOR coefficients show blueshifts for + F intensities due to very small variations of the transition energies. Meanwhile, little change is observed at the maximum point of the NOR peak, especially for –F values. In addition, the maximum of the NOR coefficient is obtained at +40 kV/cm.

In Fig. (5a and b), the SHG coefficients as a function of the photon energy for B = 0 and B = 12 T are shown for several F intensities. The positions of the resonance peak are at $E_{31}/2 \approx \hbar\omega$ (dominant-major peak) and at $E_{21} \approx \hbar\omega$ (weak-minor peak). The energy differences between these resonance peaks are presented in Table 1 for different F and B intensities. For B = 0, if we compare the position of the E_{21} and $E_{31}/2$, which are corresponding to the minimum and maximum peaks at SHG coefficient, all transition energies are almost the same for F = 0 and −10 kV/cm. This results in a single peak SHG as shown in Ref. [16]. Only the SHG coefficient is higher for F = −10 kV/cm. While the peak corresponding to E_{21} is on the left side compared to $E_{31}/2$ at F = −5 kV/cm, E_{21} peaks are on the right side for other F intensities owing to the variation of the transition energies. For B = 12 T, the SHG peaks show single value due to very small variation in transition energies according to B = 0. A blue-shift is observed when the F intensity increases in the positive direction, and at the same time, the SHG peaks are higher than the –F values. Even though very sharp effect of the positive values of F, the negative values show a very small effect on the SHG peaks and positions. In addition to all of these effects, B = 12 T value causes a very sharp decrease in the SHG owing to the variations of the absolute DMME's part ($|M_{21}M_{32}M_{31}|$) as shown in Fig. 5b.

Fig. 6 (a and b) displays the calculated THG coefficients versus the photon energy for varying F strengths for B = 0 and B = 12 T. The position of the resonance peak is at $E_{41}/3 \approx \hbar\omega$ (dominant-major peak), $E_{31}/2 \approx \hbar\omega$ (middle peak), and at $E_{21} \approx \hbar\omega$ (very weak-minor peak). For B = 0, the left (right) side peak of the THG belongs to $E_{31}/2$ (E_{21}) transition energy, and the other two transition energies are overlapped for F = 0 (5 kV/cm). The right side maximum peaks originate from $E_{41}/3$ for F = −5 and −10 kV/cm. The lower peaks are on the right for other F intensities, and the THG peak maximums decrease as positive F values increase. Since THG peaks are too small for F = ± 40 kV/cm, they are magnified 10 times (Fig. 6a).The same as the SHG coefficients, the blueshift exists for the THG coefficients with increasing + F intensities because of higher transition energies for E_{21}, $E_{31}/2$ and $E_{41}/3$ for B = 12 T. As an effect of applied B, the size of the THG peaks decreases markedly. The results show that the change in the resonance peak of the THG coefficient are both $|M_{21}M_{32}M_{43}M_{41}|$ product and in the energy interval E_{21}, E_{31}, E_{41} in the denominator. The effects on the DMMEs are related to the behavior of the electron wave function and the geometric

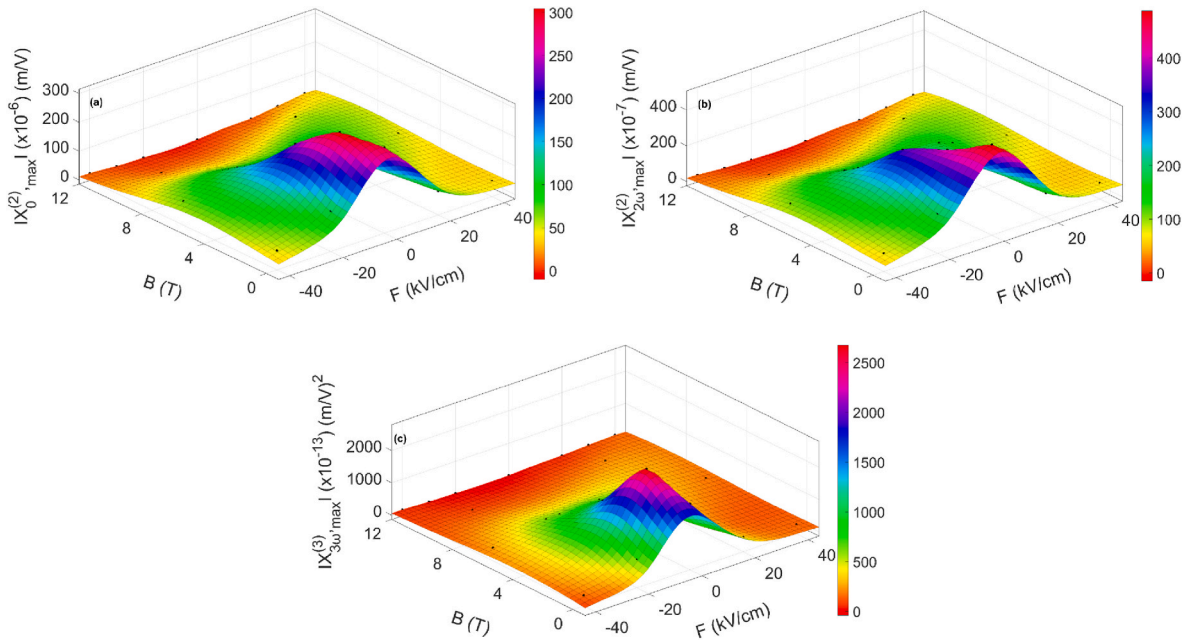

Fig. 8. Maximum of the resonance peaks of the a) NOR, b) SHG, and c) THG coefficients as a function of B (x-axis) and F (y-axis).

confinement of particles in QWs.

In Fig. 7 (a, b, and c), the NOR, SHG, and THG coefficients have been plotted as a function of the photon energy for several electric and magnetic field values. For all B values, if F = 0 is taken as a reference point, the blueshift is observed for the NOR, SHG, and THG under both positively and negatively applied F intensity. For F = 0, except for B = 0 and 4 T values, the peak values of NOR, SHG, and THGs are low and close to each other. As both F and B intensity enhances, the DMMEs change because of the overlap between the WFs. We have concluded that the position and magnitude of the resonance peaks of the NOR, SHG, and THG coefficients depend on the F and B values due to the change in the DMMEs and the energy difference.

The maximum of the peaks of the NOR, SHG, and THG coefficients versus both F and B intensities are plotted in Fig. 8, and the color scale has been added. For different F and B values, the transition energies and maximum of the NOR, SHG, and THG peaks are also given in Table 1. As derived from equations (6) and (7), the maximum of the NOR and SHG have reached maximum for low external field intensities due to being dependent only DMMEs and independent from the transition energies. As shown in Figs. 2c and 3c, while $M_{21}^2\delta_{21}$ is effective for the maximum of NOR coefficient, $M_{21}M_{32}M_{31}$ is effective for the maximum SHG coefficient. As given in equation (8), variation of the maximum of the THG coefficient is dependent to $M_{21}M_{32}M_{43}M_{41}$ which is different than the maximum of the NOR and SHG coefficient. The combined effect of large external fields reduced the effect of the DMME products and this considerably lowers the maximums of the NOR, SHG, and THG coefficients.

4. Conclusion

The finite element method, with effective mass approximation, is used to derive the wave functions and their corresponding energy levels for the $Al_xGa_{1-x}As/GaAs$ superlattice with periodically increased barrier width. The external (electric and magnetic) fields have been applied to the superlattice to modify the NOR, SHG, and THG coefficients. It is shown that the confinement of the first four energy states is highly affected by the barrier width. The magnitude and polarity (±) of applied electric field vary the probability densities of wavefunctions. It is obtained that F = −5 kV/cm intensity is the critical value for both E_{fi} and DMMEs in the case of zero B. The red/blue shift in the optical spectrum is observed as a result of the change in the transition energies. F = 40 kV/cm has been more effective to change transition energies than F = −40 kV/cm. The magnetic field provides the confinement and localization of the electrons towards the center of the superlattice. Consequently, the NOR, SHG, and THG coefficients can be tuned by changing the electric and magnetic field intensities. With the combined effect of the electric and magnetic fields, the results can be evaluated in the search for new ways to modify the electro-optical properties of semiconductor QWs.

Funding

This study is funded by Sivas Cumhuriyet University with the project number F-2021-649.

Author contribution statement

E. Ozturk and B.O. Alaydin contributed throughout the manuscript. D. Altun and O. Ozturk contributed to the introduction, data acquisition, graphic drawings, and article writing.

Declaration of competing interest

The authors declare that they have no known competing financial interests or personal relationships that could have appeared to influence the work reported in this paper.

Data availability

Data will be made available on request.

References

[1] H.-W. Hübers, H. Röser, G. Schwaab, in: Submillimetre and Far-Infrared Space Instrumentation, 1996, p. 159.
[2] J. Li, J. Li, Electric. Sci. Eng. 2 (2020) 11–25.
[3] R. Titz, M. Birk, D. Hausamann, R. Nitsche, F. Schreier, J. Urban, H. Küllman, H. Röser, Infrared Phys. Technol. 36 (1995) 883–891.
[4] I. Mehdi, in: Millimeter and Submillimeter Detectors for Astronomy II, SPIE, 2004, pp. 103–112.
[5] D. Mittleman, Sensing with Terahertz Radiation, Springer, 2013.
[6] E. Gornik, A. Andronov, Opt. Quant. Electron. 23 (1991) S267–S286.

[7] C. Sirtori, P. Kruck, S. Barbieri, P. Collot, J. Nagle, M. Beck, J. Faist, U. Oesterle, Appl. Phys. Lett. 73 (1998) 3486–3488.
[8] M. Razeghi, S. Slivken, Y. Bai, B. Gokden, S. Ramezani Darvish, New J. Phys. 11 (2009), 125017.
[9] B.O. Alaydin, Gazi Univ. J. Sci. 34 (2021) 1179–1191.
[10] B.O. Alaydin, Int. J. Mod. Phys. B 35 (2021), 2150027.
[11] A. El Aouami, M. Bikerouin, K. Feddi, N. Aghoutane, M. El-Yadri, E. Feddi, F. Dujardin, A. Radu, R.L. Restrepo, J.A. Vinasco, A.L. Morales, C.A. Duque, M. E. Mora-Ramos, Phil. Mag. 100 (2020) 2503–2523.
[12] H.V. Phuc, N.N. Hieu, L. Dinh, T.C. Phong, Opt Commun. 335 (2015) 37–41.
[13] E.C. Niculescu, M. Cristea, A. Radu, Phys. E Low-dimens. Syst. Nanostruct. 57 (2014) 138–144.
[14] M. Sayrac, Opt. Quant. Electron. 54 (2021) 52.
[15] S. Baskoutas, E. Paspalakis, A. Terzis, J. Phys. Condens. Matter 19 (2007), 395024.
[16] O. Ozturk, B. Alaydin, D. Altun, E. Ozturk, Laser Phys. 32 (2022), 035404.
[17] J.C. Martínez-Orozco, M.E. Mora-Ramos, C.A. Duque, J. Lumin. 132 (2012) 449–456.
[18] W. Xie, J. Lumin. 145 (2014) 283–287.
[19] X. Liu, L. Zou, C. Liu, Z.-H. Zhang, J.-H. Yuan, Opt. Mater. 53 (2016) 218–223.
[20] M. Karimi, A. Keshavarz, Phys. E Low-Dimens. Syst. Nanostruct. 44 (2012) 1900–1904.
[21] O. Ozturk, E. Ozturk, S. Elagoz, Chin. Phys. Lett. 36 (2019), 067801.
[22] O. Ozturk, E. Ozturk, S. Elagoz, Phys. Scripta 94 (2019), 115809.
[23] S. Baskoutas, E. Paspalakis, A.F. Terzis, Phys. Rev. B 74 (2006), 153306.
[24] G. Wang, Q. Guo, Phys. B Condens. Matter 403 (2008) 37–43.
[25] Y.-B. Yu, S.-N. Zhu, K.-X. Guo, Phys. Lett. 335 (2005) 175–181.
[26] R. Khordad, Indian J. Phys. 88 (2014) 275–281.
[27] K.-X. Guo, C.-Y. Chen, T. Das, Opt. Quant. Electron. 33 (2001) 231–237.
[28] L. Tsang, D. Ahn, S. Chuang, Appl. Phys. Lett. 52 (1988) 697–699.
[29] M.J. Karimi, A. Keshavarz, Phys. E Low-Dimens. Syst. Nanostruct. 44 (2012) 1900–1904.
[30] M. Sayrac, A. Turkoglu, M.E. Mora-Ramos, F. Ungan, Opt. Quant. Electron. 53 (2021) 485.
[31] D. Altun, O. Ozturk, B.O. Alaydin, E. Ozturk, Micro Nanostruct. 166 (2022), 207225.
[32] J. Botero, J. Shertzer, Phys. Rev. 46 (1992) R1155–R1158.
[33] S. Lepaul, A.d. Lustrac, F. Bouillault, IEEE Trans. Magn. 32 (1996) 1018–1021.
[34] K. Nakamura, A. Shimizu, M. Koshiba, K. Hayata, IEEE J. Quant. Electron. 25 (1989) 889–895.
[35] B.O. Alaydin, D. Altun, E. Ozturk, Thin Solid Films 755 (2022), 139322.
[36] M. Karimi, H. Vafaei, Superlattice. Microst. 78 (2015) 1–11.
[37] Z.-H. Zhang, J.-H. Yuan, Phys. B Condens. Matter 646 (2022), 414356.